Journal of Chemical Health Risks

www.jchr.org

JCHR (2025) 15(6), 3498-3519 | ISSN:2251-6727

Synthesis, Spectroscopic Characterization, and DFT Insights into a Ni(II) Dithiocarbamate and Its Mixed-Ligand Derivative, with Conversion of the Parent Complex to Nanocrystalline Nickel Sulfide Exhibiting Enhanced Visible-Light Photocatalytic Activity

Qudsia Rasool[1], R. Bhaskaran[1*]

[1] Department of Chemistry, Annamalai University, Annamalai Nagar, Chidambaram, Tamilnadu-608002, India, [1*] Chemistry Section, FEAT, Annamalai University, Annamalai Nagar, Tamilnadu-68002, India

(Received: 05 September 2025 Revised: 15 October 2025 Accepted: 10 November 2025)

KEYWORDS

Nickel(II)Dithiocarbamate complexes; Mixed-ligand coordination complexes; 4-Piperidinopiperidineligand;1,2-Bis(diphenylphosphino)ethane(dppe); Metal–ligandbonding; Coordination chemistry, Pxrd, Methylene blue , Rhodamine -6G.

ABSTRACT:

This study reports the synthesis, spectroscopic characterization, and functional evaluation of a novel nickel(II) dithiocarbamate complex derived from 4-piperidinopiperidine and its corresponding mixed-ligand Ni(II) complex formed with 1,2-bis(diphenylphosphino)ethane (dppe). Elements (CHNS and Ni gravimetry), FT-IR, UV-Vis, and NMR spectroscopy were used to characterise the two complexes, which were produced in good yields through salt-metathesis and ligand exchange processes. Spectral data suggest a primarily square-planar coordination environment and validate the effective chelation of phosphine and dithiocarbamate ligands to the Ni(II) core. Density Functional Theory (DFT) investigation of a model Ni(II) dithiocarbamate species gave information about electronic structure, frontier orbital distribution, and chemical reactivity indices in addition to revealing a distorted square-planar geometry. Nanocrystalline nickel sulphide (NiS) was produced by thermally breaking down the dithiocarbamate precursor. PXRD, SEM/EDS, and UV–DRS analyses revealed phase-pure β-NiS with a band gap of about 3.08 eV. NiS has the potential to be an efficient photocatalyst for the removal of organic pollutants, as evidenced by photocatalytic studies that showed significant visible-light induced degradation of model organic dyes (Methylene Blue = 85% and Rhodamine-6G ≈ 70% after 180 min). For Ni(II) dithiocarbamate complexes and their generated nanomaterials, this work offers synthesis methods, thorough characterisation, and application insight.

1. INTRODUCTION

Dithiocarbamates (DTCs) continue to attract significant research interest owing to the unique electronic characteristics of their nitrogen and sulfur donor atoms and their ability to form highly stable chelate complexes with a wide range of transition metals(1). Effective bonding with soft transition metal ions including Ni^{2+}, Cu^{2+}, Zn^{2+}, and Pt^{2+} is made possible by the strong bidentate coordination mode of the $[R_2NCS_2]^-$ ligand, which is mainly driven by the soft and polarisable sulphur atoms(2). Metal–ligand interactions are further modulated by the electronic and steric character of the substituent groups on the amine nitrogen, resulting in complexes with adjustable structural, magnetic, optical, and electrochemical properties(3). The use of transition metal dithiocarbamates in materials chemistry, bioinorganic chemistry, catalysis, and sensor development has been aided by this tunability(1,4).

Because of the coordination flexibility of DTC ligands, transition metals can take on a variety of geometries, such as square planar, tetrahedral, and octahedral, depending on the metal ion's electronic state and the ligand's steric profile(5).Prior single-crystal X-ray diffraction structural studies on complexes like [Co ($Et_2dtc)_3$], [Co($nPr_2dtc)_3$], [Pd($iPr_2dtc)_2$], and [Pd ($Et_2dtc)_2$] have shown differences in metal–sulfur bond lengths that are closely correlated with ligand bulkiness and metal identity(6). Similarly, nickel(II) dithiocarbamate complexes such as Ni($Et_2dtc)_2$ and related bis(dialkyldtc) species have been characterized by single-crystal X-ray analysis, revealing predominantly square planar geometries around the Ni center, consistent with strong chelation by two bidentate DTC ligands; these structures also show variation in Ni–S bond distances depending on the alkyl substituents, with bulkier groups generally leading to shorter Ni–S

Journal of Chemical Health Risks

www.jchr.org

JCHR (2025) 15(6), 3498-3519 | ISSN:2251-6727

contacts and enhanced stability relative to less bulky analogues(1).According to complementary UV-Vis spectroscopic analyses of stability constants, complex stability increased noticeably in the order Co < Ni < Pd(7). Also, it was discovered that the steric effects of the alkyl substituents affected stability in different ways for different metals: cobalt complexes show the trend Et > iPr > nPr > Me, while nickel and palladium complexes show increasing stability with increasing alkyl-group steric bulk (Me < Et < nPr < iPr)(6).The shortest M–S bond lengths and best stability were also shown by complexes containing the iPr_2dtc ligand, demonstrating the combined effect of steric hindrance and electronic contributions in improving metal–ligand interaction(6).

In this paper, we report the synthesis of a nickel(II) dithiocarbamate complex derived from the secondary amine, 4-piperidinopiperidine. Subsequent reaction of this Ni (DTC) species with $NiCl_2$ and 1,2-bis(diphenylphosphino)ethane (dppe) afforded a second mixed-ligand nickel (II) complex. Both the primary Ni (DTC) and the mixed-ligand complexes were subjected to comprehensive analytical characterization. Detailed spectral studies were performed, including UV–visible spectroscopy and infrared (FT-IR) analysis, as well as nuclear magnetic resonance (^1H NMR and ^{13}C NMR) spectroscopy, to elucidate their electronic, functional group, and structural features. These combined spectral and analytical data provide insight into the coordination environment and confirm the successful formation of the targeted complexes(8).

2. EXPERIMENTAL

All reagents and solvents employed in the present study were of analytical grade and were used as received without any further purification (Sd Fine Chemicals). Elemental analysis was carried out to confirm the composition of the synthesized complexes, and Ni was estimated by Ni (DMG) gravimetric analysis. Infrared spectra were recorded in the 400–4000 cm^{-1} region using an FT-IR spectrometer, while electronic absorption spectra were measured at room temperature on a UV–visible spectrophotometer. NMR measurements were carried out on a 400 MHz spectrometer using standard procedures. All instrumental techniques were operated according to standard protocols to ensure accuracy and reproducibility of the spectral and structural data.

2.2. Synthesis of complexes

2.2.1 Preparation of bis {[4-(piperidine-1yl) piperidine]carbodithioato- κ²S,S'} nickel (II); [Ni(4-pipdtc)₂] (1)

4-Piperidinopiperidine (0.4 g, 2 mmol) and carbon disulfide (1 mL, 2 mmol) were dissolved in ethanol (10 mL) under ice-cold conditions (5 °C) with constant stirring to form a yellow solution of the corresponding dithiocarbamic acid. To this solution, an aqueous solution of nickel(II) chloride (0.237 g, 1 mmol) was added dropwise under continuous stirring. The reaction mixture immediately yielded a green precipitate, which was collected by filtration, washed thoroughly with ethanol, and dried. The complex was obtained in good yield, 75%.

2.2.2. Preparation of {[4-(piperidin1-yl) piperidine]carbodithioato-κ²S,S'}(1,2-bis(diphenylphosphino)ethane- κ² P,P'] nickel(II) }chloride

The mixed-ligand nickel complex, [Ni(4-pipdtc)(dppe)Cl], was synthesized by refluxing the parent nickel dithiocarbamate complex, [Ni(4-pipdtc)₂] (0.545 g, 1 mmol), with 1,2-bis(diphenylphosphino)ethane (dppe, 0.797 g, 2 mmol) and nickel(II) chloride (0.237 g, 1 mmol) in a 1:1 mixture of acetonitrile and methanol for 3 hours. During the reaction, a reddish-pink solution was formed, indicating complex formation. The reaction mixture was cooled to room temperature, and the resulting complex was precipitated, collected by filtration, and washed thoroughly with ethanol. The complex was dried and obtained in good yield, 73%.

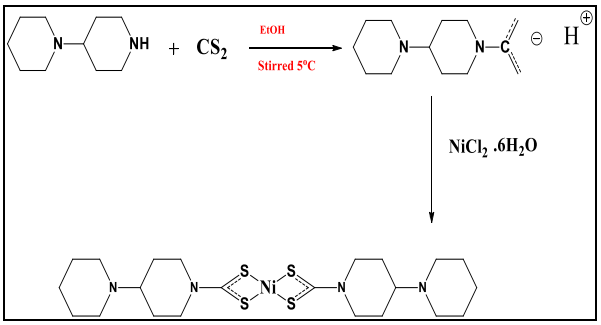

Scheme 1. Synthetic scheme of complex 1

Journal of Chemical Health Risks
www.jchr.org
JCHR (2025) 15(6), 3498-3519 | ISSN:2251-6727

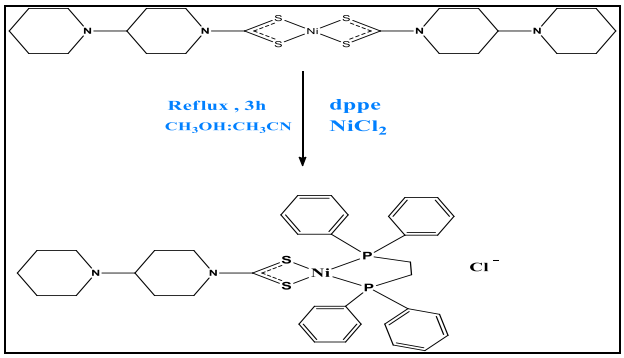

Scheme 2. Synthetic scheme of complex 2

3. RESULT AND DISCUSSION

3.1.Elemental Analysis

The empirical compositions of the mixed-ligand Ni(II) complex and the Ni(II) dithiocarbamate were verified using quantitative elemental analysis. An instrumental CHNS elemental analyser, which uses burning of the sample and subsequent measurement of combustion products to obtain accurate mass percentages of these elements, was used to determine the amounts of carbon, hydrogen, nitrogen, and sulphur(9).The purity and stoichiometry of the produced complexes were evaluated by comparing the experimental CHNS values with the computed theoretical percentages. Additionally, each complex's nickel content was measured by classical gravimetric analysis, in which the mass of the precipitated and isolated Ni(II) ion in a distinct solid state was used to determine the associated Ni percentage(10). The suggested chemical formulae for the target substances were strongly confirmed by the combined analytical data from gravimetric and CHNS methods.

Table 1. Analytical data for the Ni(II) Complexes

Compound	Ni% Exp-Cal	C% Exp-Cal	H% Exp-Cal	N% Exp-Cal	S% Exp-Cal	Melting Point ℃
$Ni(dtc)_2$ **$C_{22}H_{40}N_4NiS_4$**	10.09-10.72	48.26-48.46	7.14-7.36	10.23-10.34	23.21-23.43	150-200
2[Ni(dtc) (dppe)] Cl **$C_{37}H_{44}ClN_2NiP_2S_3$**	7.11-7.96	58.72-58.85	9.22-9.32	3.61-3.82	8.12-8.26	200-250

Table 2. Electronic and FT-IR Data (Cm^{-1})

Complex	Key λmax (nm)	ν_{C-N}	ν_{C-S}	ν_{Ni-S}	ν_{C-H}	ν_{N-H}	ν_{Ni-P}
1. [Ni(dtc)2]	250,300,350,400	1514	1000	426	2940	3402	----
2.2[Ni(dtc) (dppe)] Cl	240,310,370,450	1524	1246	531	2942	3419	512

Journal of Chemical Health Risks
www.jchr.org
JCHR (2025) 15(6), 3498-3519 | ISSN:2251-6727

3.2. IR Spectral Studies

Both the parent Ni(II) dithiocarbamate and its mixed-ligand Ni(II) complex were subjected to FT-IR spectroscopy to verify functional group participation and metal–ligand interaction; specific band locations and assignments are shown in Table 2. The coordinated secondary amine's N–H stretching vibrations are responsible for the medium-intensity absorptions seen at 3402 cm^{-1} (parent) and 3419 cm^{-1} (mixed ligand). These absorptions are consistent with typical amine N–H strains and show that the amine moiety stays intact post complexation. The CH_2 groups of the ligand backbone are the source of the aliphatic C–H stretching bands at 2940 cm^{-1} and 2941 cm^{-1}, respectively. These bands lie within the typical range for saturated hydrocarbon C–H stretches as observed in coordination complexes(11).The presence of the dithiocarbamate moiety is confirmed by the thioureide C–N stretches at 1514 cm^{-1} (parent) and 1524 cm^{-1} (mixed ligand); coordination to the metal centre usually results in shifts in this band because of delocalisation and changes in bond order upon chelation(11,12).Similar to this, C–S stretching vibrations at 1000 and 997 cm^{-1} show bidentate coordination of the sulphur donors to Ni(II). Because of metal-sulfur bonding processes, these bands are frequently found in metal dithiocarbamate complexes(2,13).Bands at 426 and 531 cm^{-1} for the parent and mixed ligand complexes, respectively, in the lower wavenumber area are attributed to Ni–S stretching modes, which are typical of Ni–S bonds in these species. The mixed-ligand complex also shows a band at 512 cm^{-1} that can be attributed to Ni–P stretching, which indicates coordination of the dppe phosphine ligand. Because of the mass and bond strength of Ni–P linkages, metal–phosphine vibrations in nickel complexes are often detected in this region(14,15). The observed shifts and precise assignments validate the successful development of both the parent and mixed-ligand complexes and support the suggested coordination settings(14).

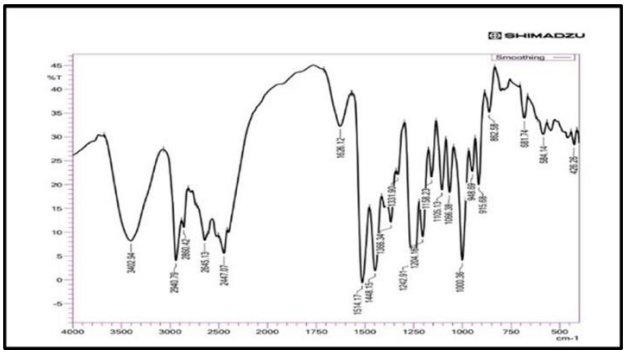

Figure. 1 FT-IR Spectra of Complex 1

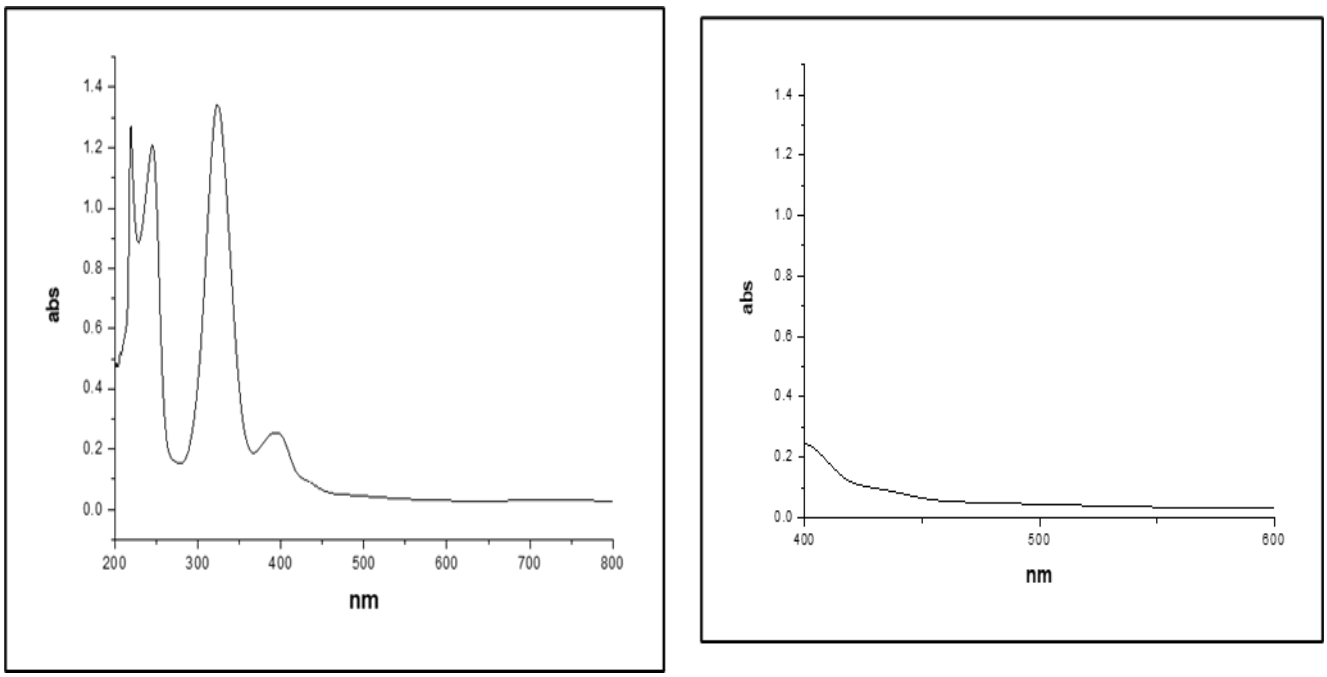

(a) UV Spectra of Complex 1 and (b) expanded spectra of Complex 1

Journal of Chemical Health Risks

www.jchr.org

JCHR (2025) 15(6), 3498-3519 | ISSN:2251-6727

3.3. Electronic Spectral Studies

The UV–Visible spectra of complexes 1 and 2 (Table 2) show intense bands in the UV region (complex 1: 250, 280, 300 and 350 nm; complex 2: ~230, 290, 330 and 390 nm) that arise from ligand-centered π→π* and n→π* transitions, confirming successful coordination. Upon coordination in a square-planar geometry, the metal d-orbitals split into distinct energy levels: the highest-energy d_{x²–y²} orbital is raised well above the other d orbitals (d_{xy}, d_{xz}, d_{yz}, d_{z²}) as a result of strong ligand interaction in the plane, producing large crystal field splitting typical of square planar complexes with a d^8 metal center like Ni^{2+}, Pd^{2+}, and Pt^{2+}. This large splitting minimizes electron-electron repulsion by keeping electrons in lower-energy orbitals and results in low-spin dsp^2 hybridization that stabilizes square planar geometry(16,17).

Because d–d transitions involve excitation between split d-orbital levels of the same metal, and are Laporte-forbidden in a centrosymmetric field, they are weak in intensity compared with ligand-centered absorptions. In this study, complex 1 shows weak d–d bands near 400 nm, ~450 nm and 700 nm, while complex 2 exhibits a weak broad band around 450 nm, all of which are assigned to these d–d transitions. The weak intensity and positions of these bands reflect the large square-planar d-orbital splitting expected for Ni^{2+} complexes, supporting a square-planar/distorted square-planar geometry for both complexes(18,19). A band in the region 350–380 nm (near 350 nm for 1 and 370 nm for 2) is attributed to ligand-to-metal charge transfer (LMCT) from sulfur to the metal. Together, the strong ligand-based transitions, LMCT, and weak d–d absorptions confirm the formation of complexes 1 and 2 and are consistent with the electronic effects of square-planar coordination(20,21). Overall, the presence of strong ligand-based transitions along with LMCT and weak d–d bands confirm the formation of complexes 1 and 2 and reflects the electronic environment created by ligand coordination(20,21,22).

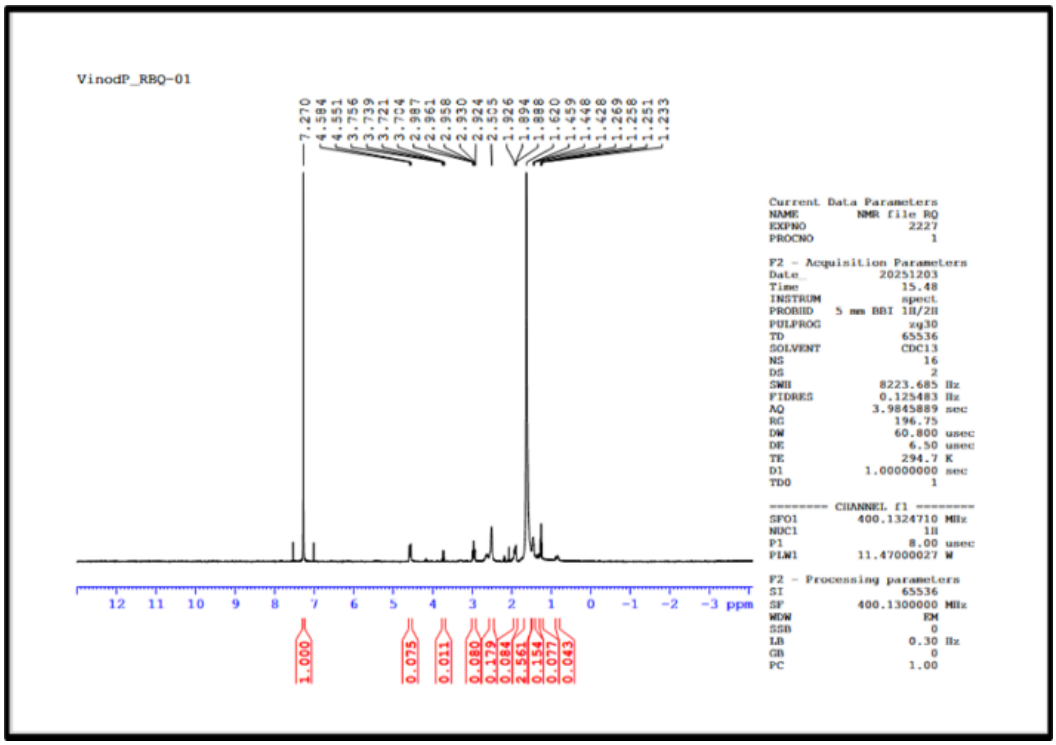

[1]H NMR Spectra of Complex 1

Journal of Chemical Health Risks
www.jchr.org
JCHR (2025) 15(6), 3498-3519 | ISSN:2251-6727

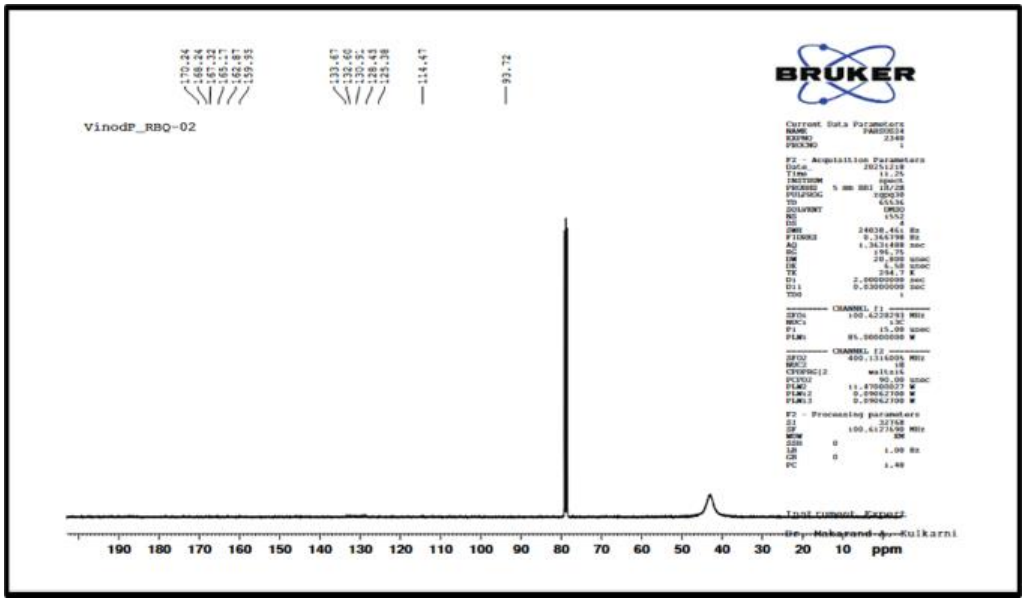

^{13}C NMR Sectra of Complex 1

3.4. ^{1}H NMR Spectral Analysis

Through the presence of expected proton environments and coordination-induced spectrum shifts, the ^{1}H NMR spectra of the parent dithiocarbamate complex and its mixed-ligand derivative offer convincing proof for the effective synthesis of the desired coordination molecules. Signals appearing downfield in the δ ~3.7–4.6 ppm region are assigned to N–CH_2 protons, which typically experience deshielding due to the electronegative nitrogen atom and show further shift changes after metal coordination because the formation of metal–ligand bonds alter the electronic density around the donor atom and adjacent protons(23). The CH_2/CH_3 protons of the ligand backbone are responsible for resonances in the aliphatic region (δ ~1.2–3.0 ppm) in both complexes, indicating that the alkyl framework is unaffected by complexation(24).In the mixed-ligand complex, additional resonances are observed in the aromatic region (δ ~7.2–8.0 ppm), confirming the presence of aryl protons from the co-ligand (such as phosphine-derived phenyl groups), and this feature clearly differentiates it from the parent complex(25).Furthermore, the slight peak shifting and broadening observed in both spectra is consistent with restricted ligand mobility, reduced rotational freedom, and changes in the chemical environment caused by coordination, which commonly leads to less sharp signals in coordination compounds when compared to free ligands(26).The residual solvent peak at δ 7.26 ppm ($CDCl_3$) is also present and is consistent with standard solvent referencing(27).Overall, the suggested structures are supported and the successful synthesis of both complexes is confirmed by the presence of distinctive aliphatic, N-linked methylene, and (in the mixed-ligand system) aromatic resonances together with coordination-related shift variations(28).

3.5.^{13}C NMR Spectral Studies

The appearance of different resonances for the thioureide carbon (NCS_2) and the expected aliphatic/aromatic carbon environments in the ^{13}C NMR spectra of both complexes provide compelling evidence for the successful formation of the dithiocarbamate framework and subsequent mixed-ligand complexation. The most diagnostic feature in both spectra is the resonance found in the downfield region (~δ 165–210 ppm), which is attributed to the dithiocarbamate moiety's thioureide carbon (C=S). Its presence verifies the formation of the NCS_2 functional group and the thioureide character resulting from resonance delocalisation between C–N and C=S, a crucial structural characteristic of metal dithiocarbamates(29).The appearance and/or slight shifting of this signal between the two complexes further supports coordination-induced electronic redistribution, since metal binding alters π-delocalization and changes shielding around the thioureide carbon(29).In the parent complex, the remaining signals mainly appear in the aliphatic region (~δ 20–65 ppm) and are attributed to

Journal of Chemical Health Risks
www.jchr.org
JCHR (2025) 15(6), 3498-3519 | ISSN:2251-6727

piperidine/piperazine type carbons, where carbons adjacent to nitrogen (N-CH_2) are typically more deshielded and appear at relatively higher δ values compared to other saturated carbons, confirming the ligand backbone, the absence or poor visibility of the thioureide carbon signal in the parent compound can be attributed to severe line broadening and reduced signal intensity arising from strong metal–sulfur coordination, rapid relaxation effects, and possible aggregation of the parent complex(30).In the mixed-ligand complex, additional signals in the aromatic region (~δ 120–150 ppm) are clearly observed, confirming the incorporation of aromatic carbon environments (e.g., phenyl groups from a phosphine ligand such as dppe), and this aromatic carbon set distinguishes the mixed-ligand system from the parent complex(31).The overall pattern of carbon resonances, including the thiocarbonyl carbon, aliphatic N-linked carbons, and (in complex-2) aromatic carbons, together with minor peak broadening/shift variations, is consistent with coordination complex formation and the expected ligand environments(32).

Table 3.^{1}H NMR spectral data of synthesized compounds

Compound	δ(ppm)	Assignment
1. [Ni(dtc)2]	4.59-3.70	N-CH_2
	3.00-2.92	CH_2(α to N)
	1.93-1.23	Remaining aliphatic CH_2
2. 2[Ni(dtc)(dppe)] Cl	7.99-7.26	Ar-H(phenyl protons)
	2.52-1.86	Aliphatic CH_2(ligand backbone)

Table 4. ^{13}C NMR spectral data of synthesized compounds

Compound	δ(ppm)	Assignment
1. [Ni(dtc)2]	170.24-165.87	C=S(thiocarbonyl carbon NCS_2)
	133.61-114.41	C-N
	40-55	Aliphatic carbons(N-CH_2)
2.2[Ni(dtc)(dppe)] Cl	150.1-124.4	Ar-C/Ar-CH
	165-210	C=S
	20-65	Aliphatic carbons (N-CH_2)

4.DFT Analysis of a Ni (II) Dithiocarbamate of Complex (3)

4.1.Geometry Optimization and MEP Analysis

The optimized geometrical structure of the complex **3** was investigated using Density Functional Theory (DFT) at the B3LYP level of theory with an appropriate basis set (LANL2DZ for Ni and 6-31G(d) for non-metal atoms). All geometries were fully optimized without imposing symmetry constraints, and frequency calculations confirmed the absence of imaginary frequencies, indicating that the obtained structure corresponds to a true minimum on the potential energy surface. The Ni(II) ion prefers a four-coordinate environment, as the optimised structure shows. One phosphorus atom from the triphenylphosphine ligand, two sulphur atoms from the bidentate dithiocarbamate ligand, and one donor atom (N or S, depending on the coordination mode) from the thiocyanate ligand make up the coordination sphere. Around the Ni(II) center, this coordination arrangement creates a distorted square planar geometry that is typical of the d^8 electronic configuration.

Bond Length Analysis

It was determined that the Ni–S bond lengths were 2.2883 Å and 2.1975 Å. The small difference between these two values confirms that the dithiocarbamate ligand is effectively chelated while also indicating a modest distortion in the coordination environment. The predicted range for Ni(II)–sulfur coordination is encompassed by these bond distances. As is typical of Ni(II)–triphenylphosphine complexes, the Ni–P bond length was determined to be 2.4124 Å, reflecting significant σ-donation from the phosphorus atom to the metal center. The thiocyanate ligand's coordination through the nitrogen atom is confirmed by the Ni–N bond distance of 1.8674 Å. Strong metal–ligand interaction is suggested by this comparatively shorter bond length. The delocalisation of electron density over the N–C–S

Journal of Chemical Health Risks
www.jchr.org
JCHR (2025) 15(6), 3498-3519 | ISSN:2251-6727

segment is indicated by the C–S bond length (1.8903 Å) and the C–N bond length (1.3934 Å) within the dithiocarbamate molecule. The shorter C–N bond length compared to a typical single bond supports partial double bond character due to resonance stabilization.

Analysis of Bond Angles

A distorted square planar geometry is evident from the bond angles surrounding the Ni(II) core. The predicted trans angles S(2)–Ni–P and S(3)–Ni–N were 175.53° and 172.55°, respectively. These values are quite near to the optimal 180° that is anticipated for a square planar configuration. Square planar coordination is further supported by the cis angles S(2)–Ni–N (93.25°), S(3)–Ni–P (94.69°), and P–Ni–N (90.85°), which are all near 90°. The chelating dithiocarbamate ligand's limited biting angle and the bulky triphenylphosphine ligand's steric hindrance are the causes of the slight departures from the ideal values. Its d^8 electronic state, which favours square planar geometry because of ligand field stabilisation effects, is consistent with the almost planar arrangement surrounding the Ni(II) center.

The formation of a stable four-coordinate Ni(II) complex with distorted square planar geometry is confirmed by the optimised geometrical parameters. Strong metal–ligand interactions and efficient chelation by the dithiocarbamate ligand are shown by the bond length and bond angle values, and overall structural stability is aided by electronic delocalisation within the ligand framework.

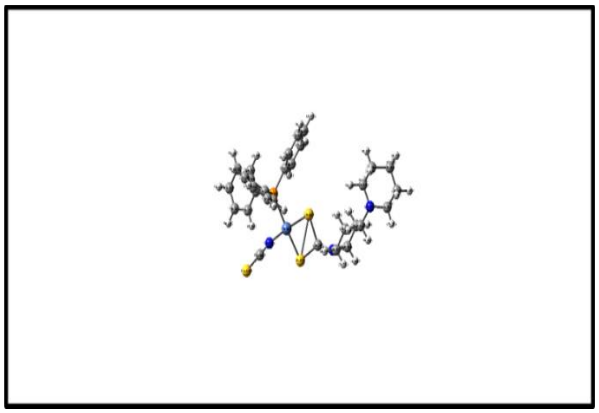

Optimized structure of complex 3

Table 3.5. Bond lengths and bond angles of complex 3

Bond Length	Calculated value(Å)	Bond Angle	Calculated value(°)
Ni-S1	2.288	S2-Ni-P	175.53
Ni-S2	2.197	S2-Ni-N	93.24
Ni-P	2.412	S3-Ni-P	94.68
Ni-N	1.867	S3-Ni-N	172.52
		P-Ni-P	90.85

4.2.Molecular electrostatic potential (MEP) surface

The Molecular Electrostatic Potential (MEP) surface of the optimized Ni(II) dithiocarbamate complex was generated to investigate the charge distribution and identify potential reactive sites within the molecule. The electrostatic potential values range from -5.842×10^{-2} a.u. to $+5.842 \times 10^{-2}$ a.u., as shown in the colour scale of the MEP map. Green denotes near-neutral potential, blue denotes positive potential, and red to orange denotes regions of negative electrostatic potential on the MEP surface. The most negative potential regions (orange to red) are located mostly over the dithiocarbamate ligand's sulphur atoms and somewhat over the thiocyanate moiety, as the MEP map makes evident. This suggests that these areas have a high electron density, proving that sulphur atoms are potent electron-donating centers. Because of this, these areas are more vulnerable to electrophilic assault.

The presence of π-electron delocalisation within the ligand backbone is supported by the moderately negative potential that is also spread along the dithiocarbamate group's N–C–S framework. This delocalisation improves coordination with the Ni(II) core and increases ligand stability. The phenyl rings' hydrogen atoms and a small area close to the metal center are the primary locations of the positive electrostatic potential regions (blue). Because it coordinates with soft donor ligands, the Ni atom's electrophilic nature is reflected in the positive potential around it. These areas might be potential locations for interactions between nucleophiles.

Because of the delocalised π-electron density throughout the aromatic system, the triphenylphosphine ligand's phenyl rings are primarily green in colour, suggesting a somewhat neutral electrostatic potential.

Journal of Chemical Health Risks
www.jchr.org
JCHR (2025) 15(6), 3498-3519 | ISSN:2251-6727

In general, the MEP analysis validates: localised high electron density over donor atoms of sulphur. In the dithiocarbamate framework, effective charge delocalisation occurs. The metal center has an electrophilic property. electronic distribution that is steady across the complex. The stability of the deformed square planar shape derived from the optimisation study is further supported by the symmetric distribution of electrostatic potential.

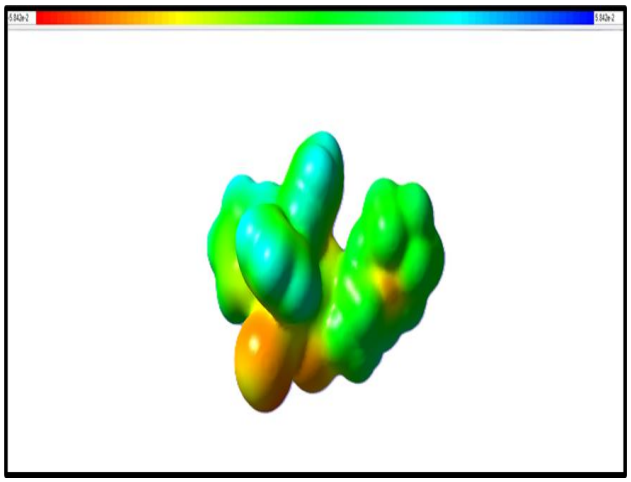

The electrostatic potential surface of complex 3

4.3. Frontier molecular orbitals

The electronic properties of the Ni(II) dithiocarbamate complex were further investigated through Frontier Molecular Orbital (FMO) analysis. The energies of the highest occupied molecular orbital (HOMO) and lowest unoccupied molecular orbital (LUMO) were calculated at the B3LYP/LANL2DZ level of theory. The HOMO energy was found to be –0.22211 a.u. (–6.04 eV), while the LUMO energy was –0.12290 a.u. (–3.35 eV). The calculated energy gap (ΔE) between HOMO and LUMO is 2.69 eV.

HOMO Analysis;

The HOMO slightly extends toward the nickel core and is mostly found over the dithiocarbamate ligand's sulphur atoms. This suggests that ligand-based orbitals with potential metal–ligand interaction characteristics have made a substantial contribution. Sulphur atoms' function as potent donor sites in coordination is confirmed by the electron density over them. According to the distribution of HOMO density, the complex is stabilised in large part by electron donation from the dithiocarbamate moiety toward the metal center.

LUMO Analysis;

The metal center receives the majority of the LUMO, with the thiocyanate and phosphine ligands receiving a smaller amount. This suggests a strong metal-centered or metal-ligand antibonding nature for the LUMO. The metal center may serve as an electron-accepting site, based on the localisation surrounding the Ni atom. This pattern suggests that metal-centered transitions or ligand-to-metal charge transfer (LMCT) may occur.

Energy Gap Interpretation;

The HOMO–LUMO energy gap of 2.69 eV indicates moderate kinetic stability of the complex. A relatively moderate energy gap suggests:

- Good thermodynamic stability
- Moderate chemical reactivity
- Controlled charge transfer ability

The gap value supports the distorted square planar geometry observed in the optimized structure and indicates effective overlap between metal and ligand orbitals.

Overall Electronic Characteristics;

The FMO analysis verifies:

- Sulphur donor atoms with strong electron density localisation (HOMO)
- The Ni(II) center's capacity to take electrons (LUMO)
- Important orbital interaction between the metal and the ligand
- Electronic arrangement that is stable but somewhat reactive

The creation of a stable four-coordinate Ni(II) complex with effective metal–ligand bonding interactions is thus supported by the electronic structure study.

Journal of Chemical Health Risks
www.jchr.org
JCHR (2025) 15(6), 3498-3519 | ISSN:2251-6727

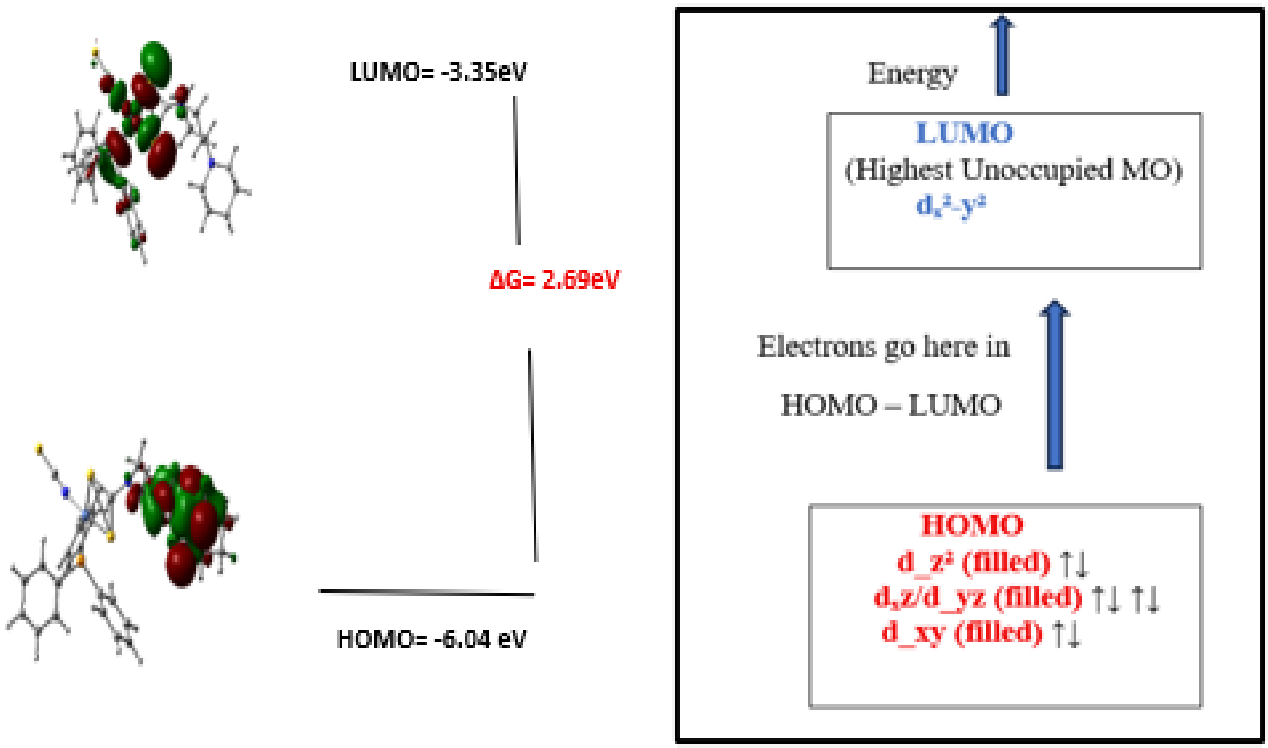

(a) HOMO and LUMO plots of complex 3 (b) Electronic Energy Level Diagram Showing HOMO–LUMO Transition

Molecular Orbital Diagram Interpretation and Correlation with DFT Studies:

The relative energy levels and electron density distribution of the frontier orbitals covered in the FMO study are graphically shown in the molecular orbital diagram created for the Ni(II) dithiocarbamate complex. As shown in the diagram, the highest occupied molecular orbitals (HOMO)which extend primarily over the filled metal–ligand bonding and nonbonding d-orbitals (including contributions from ligand sulphur donors), are shown at lower energy relative to the unoccupied orbitals. Higher energy corresponds to the antibonding d_x^2-y^2 orbital with considerable metal character, which is the lowest unoccupied molecular orbital (LUMO). The diagram's high LUMO localisation around the nickel center is consistent with the DFT LUMO analysis, which shows a metal-centered or metal-ligand antibonding character with lesser contributions from the phosphine and thiocyanate ligands.

According to the computed HOMO (–6.04 eV) and LUMO (–3.35 eV) energies acquired at the B3LYP/LANL2DZ level of theory, the arrow in the molecular orbital diagram that shows electron transfer from the HOMO to the LUMO is the direction of the border orbital transition. The diagram's HOMO–LUMO gap of 2.69 eV supports the notion that the complex is both moderately reactive and thermodynamically stable because it matches the moderate energy separation found by DFT. Furthermore, the energy ordering displayed in the MO diagram supports the distorted square-planar geometry observed from structural optimisation, as this geometry leads to a characteristic splitting pattern of the Ni(II) d-orbitals where the antibonding d_x^2-y^2 orbital lies highest in energy, consistent with the identity of the LUMO. Thus, the molecular orbital diagram not only summarises the DFT results but also correlates the electronic structure with the overall bonding framework of this four-coordinate, square-planar Ni(II) complex.

Table 5. Global chemical reactivity parameters for complex 3

Parameter (eV)	**3**
Energy (a.u)	-1534

Journal of Chemical Health Risks
www.jchr.org
JCHR (2025) 15(6), 3498-3519 | ISSN:2251-6727

E_{HOMO}	-6.04
E_{LUMO}	-3.35
Energy Gap	2.69
Ionization potential (IP)	6.04
Electron affinity (EA)	3.35
Absolute electronegativity (χ)	4.70
Absolute softness (σ)	0.74
Chemical hardness (η)	1.35
Chemical potential (μ)	-4.70
Electrophilicity (ω)	8.18

4.4. Global Reactivity Parameters and Their Chemical Significance

DFT was used to determine the synthesised complex's global reactivity characteristics based on the frontier molecular orbital energies. The optimised geometry's thermodynamic stability was confirmed by the discovery that the optimised structure's total electronic energy was -1534 a.u.

Ionization Potential and Electron Affinity

Making use of Koopman's theorem:

Potential for Ionisation (IP) = $-E_{HOMO}$ = 6.04 eV

Affinity of Electrons (EA) = $-E_{LUMO}$ = 3.35 eV

Since the complex doesn't need a lot of energy to remove electrons, electron transfer activities are made easier by the modest ionisation potential. The electron affinity value shows a favourable inclination to receive electrons, which promotes interaction with electron-rich dye molecules during photocatalysis.

Chemical Hardness and Softness

The following formulas were used to determine chemical softness (σ) and hardness (η):

$\eta = (IP - EA)/2 = 1.35$ eV

$\sigma = 1/\eta = 0.74$ eV^{-1}

While softness denotes polarisability and reactivity, chemical hardness quantifies resistance to charge transfer.

The complex is neither too soft nor too hard, as indicated by its intermediate hardness value of 1.35 eV, which suggests balanced stability and reactivity. Good polarisability is reflected in the corresponding softness (0.74 eV^{-1}), which improves adsorption and interaction with organic dye molecules. Because of their polarisable sulphur atoms, dithiocarbamate ligands, which are sulfur-donor complexes, naturally increase softness. According to HSAB principles, this explains why the complex and soft organic substrates interact well.

Electrophilicity Index

This is how the electrophilicity index (ω) was computed:

$\omega = \mu^2 / 2\eta = 8.18$ eV

Strong electron-accepting ability is indicated by a high electrophilicity rating. Given that the complex can efficiently trap photoexcited electrons and contribute to the production of reactive oxygen species (ROS), this characteristic is especially crucial in understanding photocatalytic dye degradation. The experimental photocatalytic efficiency found in this study is supported by literature reports indicating complexes with electrophilicity values above 6 eV show improved redox reactivity.

5.Characterization of Nickel sulfide nanoparticle

5.1. Powder X-ray diffraction analysis of NiS

The crystalline structure and phase purity of the nickel sulfide (NiS) sample synthesized via nickel dithiocarbamate precursor were investigated by powder X-ray diffraction (PXRD). The PXRD pattern of NiS, recorded in the 2θ range from 20° to 80°, is presented in **Fig.5.1**. A clear set of diffraction peaks is observed, indicating the formation of a crystalline phase rather than an amorphous or poorly ordered material. The standard Joint Committee on Powder Diffraction Standards (JCPDS) file No. 86-2281, which corresponds to the β-NiS (nickel sulphide) phase, was used to index the observed diffraction peaks. It is common practice to

Journal of Chemical Health Risks
www.jchr.org
JCHR (2025) 15(6), 3498-3519 | ISSN:2251-6727

verify the production of single-phase crystalline NiS in nanostructured materials using this standard reference.

At 2θ values = 30.31°,32.21°,35.70°,37.36° and 40.47° that correspond to the (101), (300), (021), (220), and (211) crystallographic planes, prominent reflections are seen corresponding to Millerite shape of the NiS. These peaks correlate with earlier studies on β-NiS materials synthesised by different chemical methods and are directly labelled on the diffraction pattern (Figure 3.20). A favoured orientation or a larger population of lattice planes contributing to diffraction in that direction is shown by the most strong peak, which occurs at ~31° (designated as the (300) plane). Significant intensity is also shown by secondary peaks like (101) and (021) that confirm the existence of a well-developed crystalline lattice. The degree of crystallinity—a fundamental quantitative metric derived from PXRD analysis—reflects the percentage of ordered domains in the sample. While some disorder, flaws, or nanoscale domains contribute to peak broadening, the material's moderate crystallinity indicates that it contains a sizable fraction of ordered lattice structures. Because of size effects and surface strain, nanostructured sulphides frequently exhibit moderate crystallinity.

Peak broadening can be further analyzed using the Scherrer equation,

$$D = \frac{K\,\lambda}{\beta\,\cos\theta}$$

where β is the full width at half maximum (FWHM) of the chosen peak adjusted for experimental broadening, θ is the Bragg angle, K is the form factor (usually 0.9), D is the average crystallite size, and λ is the Cu Kα radiation wavelength (1.5418 Å). The average crystallite size calculated using the Scherrer equation was found to be 47.22 nm. In accordance with the broad peak profiles, an estimate of the crystallite size in the nanometre zone can be obtained by applying this equation to the most intense diffraction peak. This kind of widening usually indicates microstrain or tiny coherent diffraction domains inside the crystalline lattice. Significantly, there are no extra reflections in the PXRD pattern that might be ascribed to secondary phases such elemental sulphur, nickel oxides, or leftover precursor species. By showing that the breakdown of the nickel dithiocarbamate precursor produces a single crystalline sulphide phase under the applied conditions, the lack of extraneous peaks validates the phase purity of the synthesised NiS. This observation is consistent with observations in the literature that NiS synthesised chemically only displayed the distinctive β-NiS phase reflections when indexed against JCPDS standards.

In conclusion, the effective synthesis of crystalline NiS is confirmed by PXRD analysis. The computed crystal size of 47.22 nm indicates a material with notable organised domains scattered with nanocrystalline features, and the indexed diffraction pattern exactly matches standard reference data (JCPDS No. 86-2281). Understanding the material's future physicochemical properties and possible functional performance in applications like energy storage, electrical devices, and catalysis depends on these structural features.

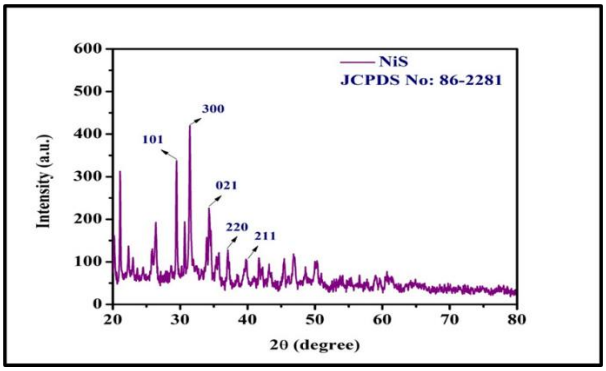

Fig.5.1. Powder X-ray diffraction pattern of NiS

Dislocation Density Analysis

In addition to crystallite size estimation, the dislocation density (δ), which provides insight into the defect concentration within the crystal lattice, was evaluated**.** Dislocation density, which is an important indicator for evaluating structural flaws in nanocrystalline materials, is the total length of dislocation lines per unit volume. The following relation can be used to estimate it:

$$\delta = 1/D^2$$

where *D* is the crystallite size expressed in meters. Substituting the calculated crystallite size (47.22×10^{-9} m) into the above equation, the dislocation density was determined to be: $\delta = 4.48 \times 10^{14}$ lines m^{-2}. The resultant value falls within the usual range that has been documented for sulphide materials with nanostructures. The existence of lattice flaws such vacancies, edge dislocations, and grain boundary defects is indicated by a comparatively higher dislocation density. These flaws

Journal of Chemical Health Risks
www.jchr.org
JCHR (2025) 15(6), 3498-3519 | ISSN:2251-6727

are caused by internal lattice strain effects and decreased particle size in nanocrystalline systems. By creating more active sites and promoting better charge carrier separation, such structural flaws might increase surface reactivity. As a result, the computed dislocation density enhances the structural data obtained from PXRD analysis and further validates the synthesised NiS nanocrystalline nature.

Lattice Parameter Determination

To further validate the crystal structure of the synthesised Nickel sulfide sample, lattice parameters were determined from multiple indexed reflections in the PXRD pattern. The interplanar spacing (d) corresponding to the prominent diffraction peaks at 2θ = 30.31° (101), 32.21° (300), 35.70° (021), and 37.36° (220) was calculated using Bragg's law: d= λ /2sinθ. where λ = 1.5418 Å (Cu Kα radiation) and θ is the Bragg angle.

The calculated d-spacings were subsequently substituted into the hexagonal lattice equation:

$$\frac{1}{d^2} = \frac{4}{3}\frac{(h^2 + hk + k^2)}{a^2} + \frac{l^2}{c^2}$$

For the (300) reflection (where $l = 0$), the equation simplifies to:

$$\frac{1}{d^2} = \frac{12}{a^2}$$

Using the experimentally determined d-spacing for the (300) plane, the lattice constant $a$was calculated to be: $a = 9.64A^{\circ}$.Substitution of this value into the lattice equation corresponding to the (101) reflection enabled determination of the lattice constant c, which was found to be: $c = 3.15\text{A}^{\circ}$.

For the hexagonal β-NiS (Millerite-type) phase, the obtained lattice parameters are in excellent agreement with standard reference data (JCPDS No. 86-2281), whose reported values are around a=9.62 a=9.62 Å and c=3.15 c=3.15 Å. Less than 0.5% separates the experimental and standard values, falling within allowable computational and instrumental error bounds. Phase-pure β-NiS with intact crystallographic symmetry was successfully formed, as evidenced by the close agreement between computed and reference lattice characteristics. Moreover, the low variance implies that the precursor decomposition process did not result in any notable macroscopic structural distortion.

5.2.UV-vis diffuse reflectance spectroscopy analysis of Nickel sulfide nanoparticle

The optical properties and electronic band structure of the synthesized NiS sample were investigated using UV–visible diffuse reflectance spectroscopy (UV–DRS). Diffuse reflectance measurements were performed in the wavelength range corresponding to photon energies from approximately 2 eV to 6 eV. The raw reflectance data, collected as percent reflectance (%R), were converted to the Kubelka–Munk function F(R) to account for scattering effects inherent in powdered samples. The Kubelka–Munk transformation, defined as:

$$F(R) = \frac{(1-R)^2}{2R}$$

enables the estimation of the absorption coefficient for diffuse samples and facilitates analysis of electronic transitions. To find the material's optical band gap, a Tauc plot was created by graphing (F(R)·hν)1/2 (F(R)·hν)1/2 against photon energy hν. In line with other research on transition metal sulphides, this methodology assumes an indirect permitted transition for NiS.The resulting Tauc plot from the diffuse reflectance spectra of NiS is shown in Figure 3.21. The red line represents the linear segment in the absorption edge region, which was extrapolated to intersect the energy axis. The optical band gap energy, or Eg E g, is represented as the intercept of this linear fit with the photon energy axis. Based on this analysis, the NiS sample's optical band gap was found to be 3.08 eV.

Compared to numerous values published for bulk NiS and nanostructured forms in previous publications, the derived band gap is relatively greater. For instance, depending on the synthesis technique, morphology, and particle size, hexagonal and nanostructured NiS frequently show band gaps in the range of ~2.8–3.6 eV, with smaller nanocrystals showing values as high as ~3.12 eV. Conversely, it has been found that bulk nickel sulphide materials have lower band gaps of ~2.1–2.4 eV, albeit these values vary based on defect density and stoichiometry.The relatively high band gap obtained in the present study may be attributable to the small crystalline domain size and structural disorder inherent

Journal of Chemical Health Risks
www.jchr.org
JCHR (2025) 15(6), 3498-3519 | ISSN:2251-6727

to the synthesized sample. Quantum confinement effects, common in nanoscale semiconductors, often increase the effective band gap as particle size decreases, as has been noted in various nickel sulfide nanostructures.

The observed sharp increase in (F(R)·hν)1/2 (F(R)·hν)1/2 with photon energy raising further points to a substantial optical absorption onset in the near-UV region. This characteristic suggests that the material may effectively absorb high-energy photons, which could have consequences for applications in photocatalysis, UV photodetection, or optoelectronic devices where regulated band gap energies are essential. The current material's nanostructured and potentially defect-rich nature results in a noticeably greater optical gap than classical NiS, which is commonly characterised as a smaller band gap semiconductor or even metallic depending on stoichiometry.

In conclusion, the Tauc plot of Kubelka–Munk transformed reflectance data indicates that the synthesised NiS has an optical band gap of 3.08 eV, which is confirmed by the UV–DRS analysis. This comparatively large band gap offers important quantitative information about the material's optical properties and possible functional performance. It also shows a substantial alteration of the electronic structure in comparison to bulk NiS, most likely as a result of disorder, lattice strain, and nanoscale effects.

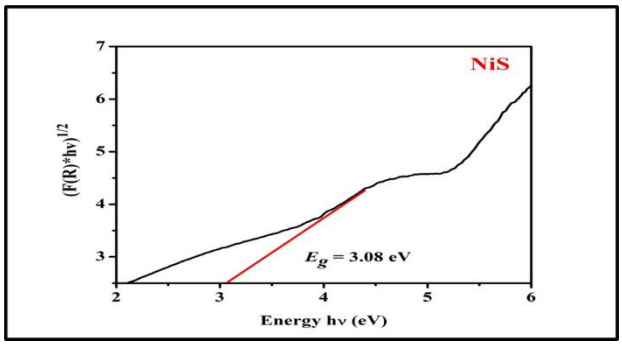

Kubelka-Munk plot of [F(R)hv]2 against hv (eV) for NiS

Urbach Energy Analysis

In addition to band gap estimation, the degree of optical disorder in the synthesised NiS sample was evaluated through Urbach energy (E_u) analysis. Urbach energy provides information about localised electronic levels within the forbidden gap, defect states, and structural disorder. It is represented by the breadth of the exponential absorption tail close to the band edge. The Urbach region follows the relation:

$$\alpha=\alpha_0 \exp(h\nu/E_u)$$

where α is the absorption coefficient, hν is the photon energy, and E_u is the Urbach energy. For diffuse reflectance data, the Kubelka–Munk function F(R) was used as an approximation of the absorption coefficient. By taking the natural logarithm of F(R), the above expression can be rewritten in linear form:

$$\ln(F(R))=h\nu/E_u+\text{constant}$$

A plot of ln(F(R)) versus photon energy (hν) in the absorption edge region (approximately 3.0–3.3 eV) exhibited a linear behaviour. The Urbach energy was determined from the inverse of the slope of this linear region and was found to be approximately 0.21 eV. The obtained Urbach energy value indicates that the NiS lattice contains localised defect states and considerable structural disorder. This finding further supports the synthesised material's nanocrystalline and defect-influenced character by showing a strong correlation with the microstrain and dislocation density determined by PXRD investigation. Such band tail states could have an impact on charge carrier dynamics and help explain NiS observed optical and photocatalytic characteristics.

5.3.SEM and EDS Analysis

The surface morphology and microstructural features of the NiS sample were examined using scanning electron microscopy (SEM). Representative micrographs at different magnifications are shown in **Fig.5.3(a)** and **(b)**, corresponding to 7,000× and 5,000× magnification, respectively. SEM provides information on particle size, shape, agglomeration, and surface texture, which are critical for understanding material behaviour in potential applications such as catalysis, energy storage, and sensing. The synthesised NiS sample is made up of irregularly shaped nanoparticles that have collected into bigger clusters, as shown by the SEM pictures. Significant particle–particle interaction occurs during the growth and nucleation phase, as seen by the dense, interconnected networks formed by individual particles rather than their isolation. The surface roughness seems rough and uneven at higher magnification (7,000×), and the particle surfaces have many tiny protrusions. In electrochemical applications, this roughness suggests a

Journal of Chemical Health Risks
www.jchr.org
JCHR (2025) 15(6), 3498-3519 | ISSN:2251-6727

high surface area morphology, which is advantageous for boosting surface-dependent characteristics like charge transfer or catalytic activity.

Instead of having consistent spherical or rod-like geometries, the detected particles exhibit a wide range of sizes and shapes. Submicron-sized grains seem to make up the majority of clusters, giving them a sponge-like shape with surface imperfections and interstitial spaces. These characteristics are typical of materials that have limited crystal development after fast nucleation, which frequently results in agglomerated nanostructures with large concentrations of surface defects. The overall morphology shows that a fine, granular material with a considerable amount of structural roughness was created by the synthesis process. Because of improved light absorption and reactive site availability, this granular assembly offers potential benefits for applications like photocatalysis that call for a larger active surface area. Furthermore, the degree of agglomeration observed at both magnifications indicates that, although the sample is mostly composed of nanoparticles, bigger clusters were formed during drying or synthesis due to high interparticle adhesion interactions. The material's conductivity, diffusion routes, and porosity may all be impacted by this clustering behaviour.

To put it simply up, SEM analysis shows that the NiS sample made using the nickel dithiocarbamate precursor has a high surface area morphology that is heterogeneous and made up of irregularly shaped, densely packed nanoparticles. It is anticipated that these structural features will improve functional performance in applications where charge transport and surface interactions are crucial.

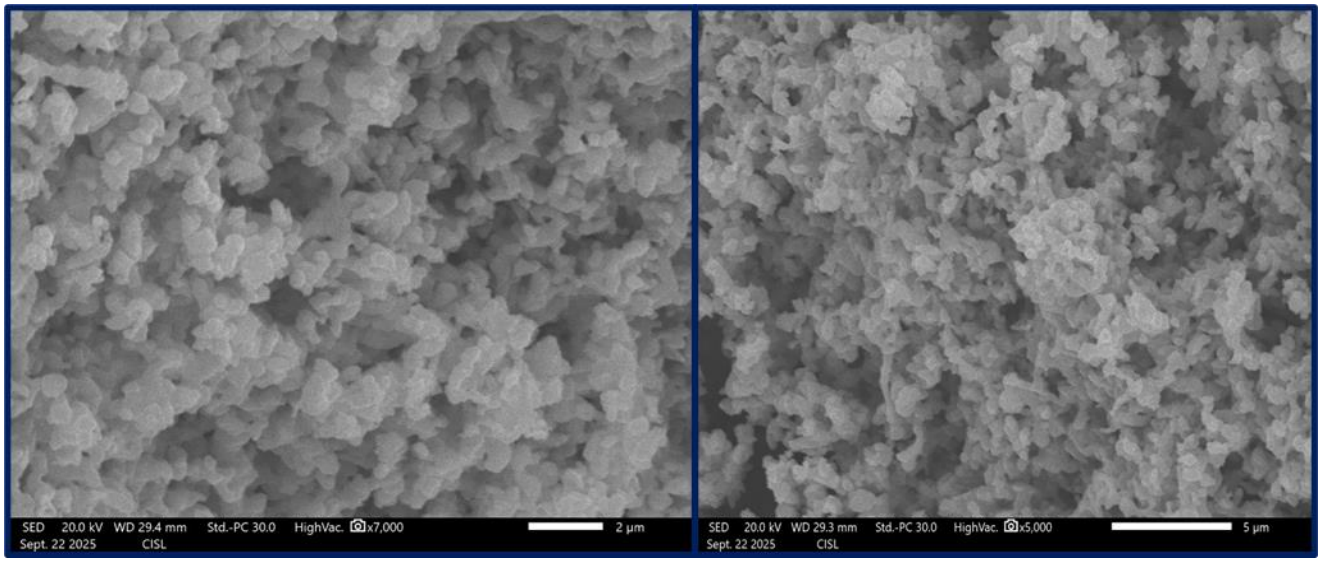

(a) (b)

Fig.5.3.(a) and (b) SEM images of NiS

The representative EDS spectrum is shown in **Fig.3.23**. EDS provides semi-quantitative elemental analysis of the sample surface, allowing verification of the constituent elements and assessment of compositional uniformity. The graph labels the significant peaks in the spectrum that correspond to sulphur (S) and nickel (Ni). Ni is the source of the strongest signals, with the largest count seen at the distinctive Ni Kα energy (~7.5 keV) and other Ni peaks at lower energies. Multiple Ni peaks confirm that nickel is the sample's main constituent. With significant peaks at its characteristic energy locations (~2.3 keV), sulphur is easily recognised, showing that it has been incorporated into the material's lattice. Within the detection range (0–20 keV), no notable peaks attributed to other elements, such as carbon, oxygen, or metals from remaining precursor species, were seen. The lack of unnecessary elemental signals indicates that the synthesised material is chemically clean and has very

Journal of Chemical Health Risks
www.jchr.org
JCHR (2025) 15(6), 3498-3519 | ISSN:2251-6727

little surface impurity contamination. This finding supports the successful development of nickel sulphide with few secondary phases and is in line with the anticipated Ni:S proportion.

The spectrum's quantitative examination reveals that, as would be expected for a stoichiometric NiS molecule, Ni and S are present in same atomic percentages. Surface roughness, local compositional fluctuations, and the intrinsic constraints of EDS quantification, especially for light elements, can cause slight departures from the optimal 1:1 atomic ratio. Nonetheless, the material's primary composition of Ni and S is confirmed by the general stoichiometry suggested by the measured intensities. The result that Ni and S are uniformly distributed throughout the sampled region, showing uniform elemental dispersion at the microstructural scale, is further supported by spatial EDS mapping. This homogeneity shows that the synthesis method produced a homogenous nickel sulphide phase, which is crucial for consistent physicochemical qualities.

EDS examination confirms that the synthesised sample is mostly composed of Ni and S in the anticipated stoichiometric proportions, with no discernible contamination from other elements. These findings support the effective synthesis of high-purity NiS with a consistent elemental distribution, as do SEM morphological observations and XRD phase identification.

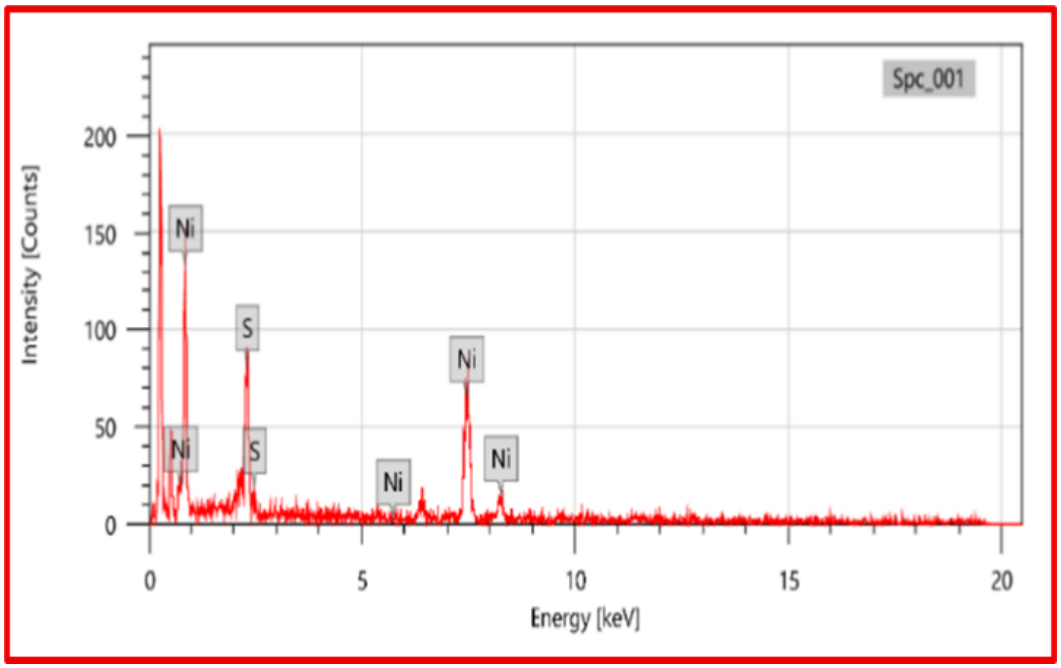

Energy dispersive X-ray spectra of NiS

5.4. Structure–Property Correlation Analysis of NiS

The structural, morphological, compositional, and optical characterisation results collectively provide a comprehensive understanding of the physicochemical nature of the synthesised Nickel sulfide sample. A systematic correlation between PXRD, UV–DRS, SEM, and EDS findings reveals a coherent structure–property relationship within the material.

The synthesis of phase-pure β-NiS with lattice parameters (a = 9.64 Å and c = 3.15 Å) was validated by PXRD analysis, which showed excellent agreement with JCPDS reference data (No. 86-2281). The dislocation density value of 4.48×10^{14} lines m^{-2} and the calculated crystallite size of 47.22 nm show the presence of nanoscale crystalline domains with structural flaws such grain boundaries and lattice faults. In nanocrystalline sulphides synthesised via precursor breakdown processes, such fault patterns are common. The optical behaviour observed in the UV-DRS analysis is directly correlated with these structural features. Nanoscale crystallite size and related structural disorder are responsible for the optical band gap of 3.08 eV, which is significantly larger than that of bulk NiS. The existence

Journal of Chemical Health Risks
www.jchr.org
JCHR (2025) 15(6), 3498-3519 | ISSN:2251-6727

of localised defect states and band tailing close to the absorption edge is further supported by the Urbach energy value of 0.21 eV. The synthesised material's defect-influenced electrical structure is strongly supported by the agreement between the optical disorder indicated by Urbach energy and the structural disorder deduced from dislocation density analysis.

SEM micrographs revealed densely packed, asymmetrically structured nanoparticles that formed agglomerated clusters with a rough surface roughness. The nanocrystalline size determined by PXRD investigation is consistent with this shape. A high density of surface-active sites, which is typical of materials with moderate crystallinity and defect-rich domains, is suggested by the granular and linked particle network shown in SEM. The nanoscale crystallite size ascertained by Scherrer analysis is likewise consistent with the observed agglomeration tendency. With only nickel and sulphur signals and no discernible impurities, the EDS results validated the sample's elemental purity and stoichiometric composition. The phase purity determined by PXRD is supported by the lack of superfluous elemental peaks. The homogenous development of the NiS phase throughout the sample is further supported by the homogeneous elemental distribution seen in EDS mapping.

The effective synthesis of structurally coherent and compositionally consistent NiS with nanoscale characteristics and defect-mediated electronic properties is confirmed by the high agreement between these independent characterisation approaches. Before assessing the material's functional performance, this comprehensive interpretation provides a strong basis for comprehending its inherent properties. These correlated structural and electronic features provide the basis for evaluating the functional behaviour of the synthesised material.

5.5.Evaluation of photocatalytic activity of NiS

The photocatalytic performance of the synthesized NiS material was assessed by monitoring the degradation of two model organic dyes — Methylene Blue (MB) and Rhodamine-6G (RG6) — under visible light illumination. These dyes were selected due to their well-established absorption features and frequent use as probe molecules for photocatalytic evaluation in aqueous media. RG6 and MB stock solutions were made independently by dissolving each dye in distilled water to a concentration of 1.0×10^{-1} M. This concentration was selected to preserve circumstances pertinent to ambient contaminant levels while guaranteeing detectable absorbance in the UV-Vis range.

For every dye, 50 millilitres of the corresponding stock solution were put into a jacketed photoreactor that had a visible light source (400–700 nm). To create adsorption–desorption equilibrium between the dye molecules and the catalyst surface, the NiS photocatalyst (dosage usually 0.5–1 g L^{-1}) was dissolved into the dye solution and magnetically agitated in the dark for 30 minutes before irradiation. The observed drops in dye concentration during illumination are guaranteed to be the result of photocatalytic processes rather than straightforward adsorption thanks to this dark equilibration step. A small amount of the suspension—usually 3–5 mL—was taken out at the conclusion of the dark phase in order to capture the initial absorbance spectrum. After that, the photoreactor was exposed to the visible light source, and during the irradiation time, aliquots were taken out at regular intervals (such as 30, 60, 90, 120, 150, and 180 minutes). After removing photocatalyst particles with a centrifuge, the UV-Vis absorbance spectrum of each aliquot was recorded.

The distinctive absorption peak centred at 664 nm was used to follow the MB degradation **Fig.5.5.(a)**. The strongest intensity is seen in the first spectra, which was taken right after the dark equilibration (t = 0). Peak intensity systematically decreases with increasing irradiation time, suggesting that MB molecules gradually photodegrade in the presence of light and NiS. The MB absorption peak exhibits a notable decrease in intensity during 180 minutes of exposure to visible light, indicating the NiS photocatalyst's efficient photocatalytic activity. Similarly, the absorbance peak at 526 nm was used to track the photocatalytic degradation of RG6 **Fig. 5.5.(b)**. As the exposure duration rises from 0 to 180 minutes, the peak intensity of the RG6 spectra shows a time-dependent decline. The RG6 band's gradual attenuation indicates that NiS can aid in Rhodamine-6G's degradation in the presence of applied visible light.

Journal of Chemical Health Risks
www.jchr.org
JCHR (2025) 15(6), 3498-3519 | ISSN:2251-6727

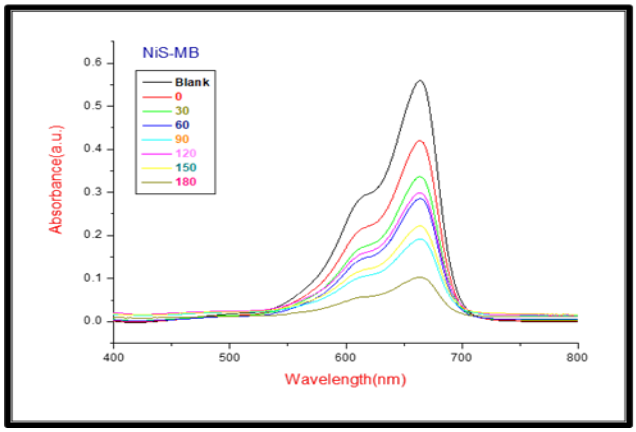

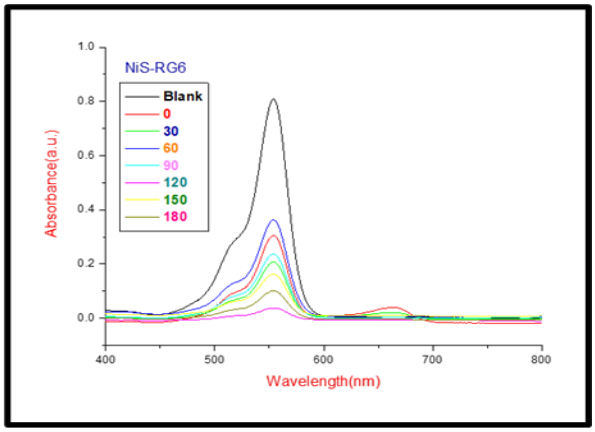

Fig.5.5.(a) and(b) Time-dependent UV-vis absorption spectra for photodegradation of methylene blue and rhodamine-6G in the presence of as-prepared nickel sulfide nanoparticle under ultraviolet light.

The photocatalytic degradation efficiency (%) for each dye was calculated using the expression:

$$\text{Degradation efficiency}(\%) = \frac{C_0 - C_t}{C_0} \times 100$$

where $C_0$is the initial dye concentration after dark equilibration, and $C_t$is the concentration at irradiation time t, determined from the change in absorbance according to the Beer–Lambert law.

At the end of 180 min of visible light irradiation, the absorbance peak of MB decreased significantly, corresponding to an approximate 85 % degradation of the dye and Under the same conditions, RG6 also showed substantial decomposition, with an estimated 70 % degradation after 180 min of irradiation.

Both MB and RG6 are degraded over the course of the irradiation period, according to the time-dependent degradation profiles, with the absorbance intensity declining nearly monotonically. Plotting ln (C0/Ct) ln(C0) can be used to approximate the rate of degradation. To assess apparent kinetic constants under pseudo-first-order reaction assumptions, plot /C t vs time. Such kinetic analysis offers insight into the underlying photocatalytic mechanisms and enables direct comparison of catalyst performance with that reported in related investigations.

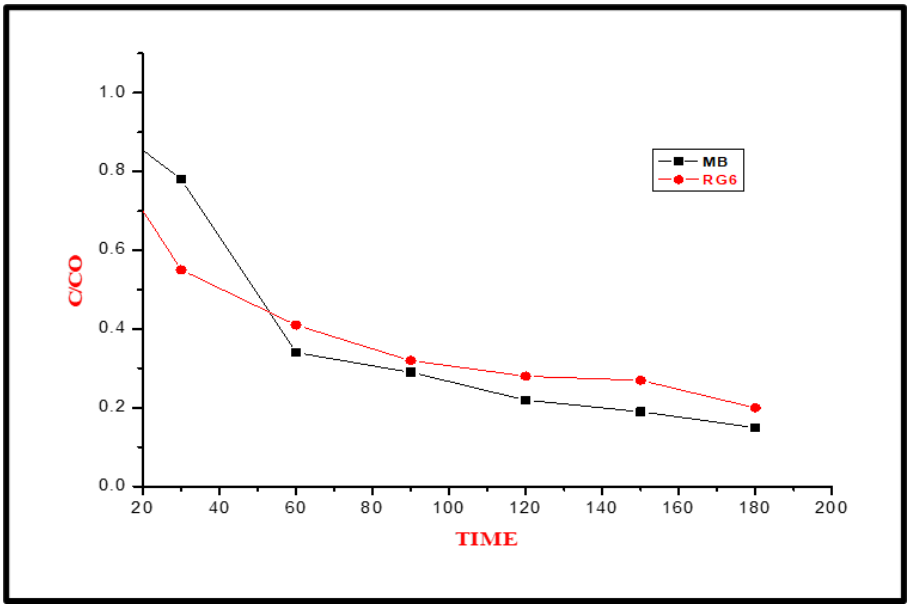

Photodegradation of methylene blue and rhodamine-6G in the presence of as-prepared nickel sulfide nanoparticles.

Journal of Chemical Health Risks

www.jchr.org

JCHR (2025) 15(6), 3498-3519 | ISSN:2251-6727

Progressive photocatalytic decomposition under visible light is confirmed by the exhibited degradation curves for both dyes (Figure 3.24.), which demonstrate a steady decline in normalised concentration (C/C_0) with increasing irradiation time. In contrast to Rhodamine-6G, Methylene Blue shows a faster drop, suggesting that the NiS catalyst degrades MB more easily. The normalised concentration of MB approaches a much lower value than that of RG6 after 180 minutes of illumination, further indicating the much better photocatalytic effectiveness of NiS toward MB under the experimental conditions. The successful activation of NiS under visible light and its capacity to produce reactive species that break down organic dye molecules are confirmed by the observed drop in absorbance peaks with irradiation time. According to literature findings on metal sulfide-based semiconductors exhibiting light-driven oxidation and reduction processes, NiS acts as an active visible-light photocatalyst, as evidenced by the effectiveness of photocatalytic degradation for both MB and RG6.

According to the results, NiS promotes effective charge separation and transfer to molecular oxygen and water through its suitable band gap and high surface area morphology. This results in reactive oxygen species like superoxide anions ($O_2\cdot^-$) and hydroxyl radicals ($\cdot OH$), which target and degrade chromophoric dye structures. Both the inherent photocatalytic effectiveness of NiS and substrate characteristics (such as molecular structure and adsorption affinity) affect the unique absorption decay behaviour for each dye.

Furthermore, because of its cationic character and stronger electrostatic interaction with the NiS surface, which promotes better adsorption and faster electron transfer, it has a higher degrading efficiency toward MB. As millerite NiS has a large number of active surface sites and short charge carrier diffusion paths, which reduces electron–hole recombination. Positively charged holes are left behind when electrons are stimulated from the valence band to the conduction band by exposure to visible light. These photogenerated charge carriers take part in surface redox processes, in which valence band holes oxidise water or hydroxide ions to produce $\cdot OH$ radicals, and conduction band electrons reduce dissolved oxygen to produce $O_2\cdot^-$ radicals.

The conjugated π-electron systems of dye molecules are targeted by these extremely reactive species, which gradually break down the chromophoric groups and eventually mineralise into smaller, less hazardous compounds. Rhodamine-6G's more complicated molecular structure and steric hindrance, which might reduce adsorption efficiency and postpone oxidative cleavage, may be the cause of its comparatively slower decomposition. Overall, the robust visible-light-driven photocatalytic performance of millerite NiS is confirmed by the combined effects of an appropriate band gap energy, a favourable surface shape, and effective charge carrier dynamics.

In addition to showcasing the as-prepared NiS intrinsic activity toward model dye contaminants, the notable visible-light photocatalytic degradation of MB (~85%) and RG6 (~70%) highlights its potential use in environmental cleanup of contaminated water. Because visible-light active photocatalysts can effectively use a larger portion of the solar spectrum to generate reactive oxygen species (such as hydroxyl radicals and superoxide anions) that mineralise persistent organic contaminants into less toxic compounds, they have been extensively studied as sustainable advanced oxidation processes for water treatment. These systems have demonstrated a great deal of ability to break down a variety of water contaminants, such as pesticides, synthetic dyes, pharmaceutical residues, and other stubborn organics that conventional wastewater treatment methods frequently are unable to fully eliminate. A promising route for solar-driven purification of industrial effluents and contaminated natural waters under environmentally relevant conditions is provided by the utilisation of visible light, including natural sunlight, which also improves the energy efficiency and applicability of photocatalytic water treatment technologies.

6.CONCLUSION

In summary, the design, synthesis, and thorough characterisation of a nickel(II) dithiocarbamate complex and its mixed-ligand derivative with a phosphine co-ligand were successfully proven in this study. While DFT investigations offered important information about electronic structure, bonding interactions, and chemical reactivity, spectral analysis (FT-IR, UV–Vis, $^1H/^{13}C$ NMR) confirmed ligand coordination and square-planar

Journal of Chemical Health Risks

www.jchr.org

JCHR (2025) 15(6), 3498-3519 | ISSN:2251-6727

Ni(II) environments. The dithiocarbamate precursor was successfully transformed into nanocrystalline NiS with verified phase purity, nanoscale dimensions (~47 nm), and notable structural disorder that contributed to special optical characteristics like an enlarged band gap (~3.08 eV). The homogenous elements distribution and high surface roughness typical of nanostructured materials were revealed by SEM/EDS investigations. Functionally, the produced NiS showed strong photocatalytic activity driven by visible light, attaining significant degradation efficiencies for typical dye pollutants when exposed to radiation. These findings suggest the wider use of Ni(II) dithiocarbamates as adaptable building blocks for functional nanomaterials and highlight the potential of NiS produced from organometallic precursors for environmental remediation applications. When considered collectively, the results support important connections between material structure, molecular coordination chemistry, and photocatalytic activity, providing interesting avenues for further research and use of complexes based on dithiocarbamates and their associated nanostructures.

Declaration of competing interest

The authors declare that they have no known competing financial interests or personal relationships that could have appeared to influence the work reported in this paper.

Data availability

Data will be available upon request.

REFERENCES

1. Ajiboye, T. O., Ajiboye, T. T., Marzouki, R., & Onwudiwe, D. C. (2022). The versatility in the applications of dithiocarbamates. *International journal of molecular sciences*, *23*(3), 1317.
2. Odularu, A. T., & Ajibade, P. A. (2019). Dithiocarbamates: challenges, control, and approaches to excellent yield, characterization, and their biological applications. *Bioinorganic Chemistry and Applications*, *2019*(1), 8260496.
3. Andrew, F. P.; Ajibade, P. A. Metal Complexes of Alkyl–Aryl Dithiocarbamates: Structural Studies, Anticancer Potency and Applications as Precursors for Nanocrystals. Coord. Chem. Rev. 2018.
4. Pugh, D., & Hogarth, G. (2025). Addressing misconceptions in dithiocarbamate chemistry. *Dalton Transactions*.
5. Van Gaal, H. L. M., Diesveld, J. W., Pijpers, F. W., & Van der Linden, J. G. M. (1979). Carbon-13 NMR spectra of dithiocarbamates. Chemical shifts, carbon-nitrogen stretching vibration frequencies and. pi.-bonding in the NCS2 fragment. *Inorganic Chemistry*, *18*(11), 3251-3260.
6. Tarique, M., & Aslam, M. (2016). Comparative study on the IR spectra of some transition metal dithiocarbamates. *Biosciences Biotechnology Research Asia*, *5*(2), 833-836.
7. Singh, R. P., Maurya, V. K., Maiti, B., Siddiqui, K. A., & Prasad, L. B. (2018). Three new homoleptic nickel (II) 1, 1-dithiocarbamate complexes: synthesis, structure, electrical conductivity and DFT study. *Journal of Coordination Chemistry*, *71*(16-18), 3008-3020.
8. Pal, S. K., Singh, B., Yadav, J. K., Yadav, C. L., Drew, M. G., Singh, N., ... & Kumar, K. (2022). Homoleptic Ni (II) dithiocarbamate complexes as pre-catalysts for the electrocatalytic oxygen evolution reaction. *Dalton Transactions*, *51*(34), 13003-13014.
9. Singh, A., Kumar, R., Shiv, K., Pandey, S. K., Bharty, M. K., Butcher, R. J., & Prasad, L. B. (2024). Synthesis, crystal structure and screening for anticonvulsant and antianxiety activities of three new Ni (II), Cu (II), and Zn (II) dithiocarbamate complexes. *Journal of Molecular Structure*, *1298*, 137052.
10. Lakshmanan, P., Thirumaran, S., & Ciattini, S. (2020). Synthesis, spectral and structural studies on NiS2PN and NiS2P2 chromophores and use of Ni (II) dithiocarbamate to synthesize nickel sulfide and nickel oxide for photodegradation of dyes. *Journal of Molecular Structure*, *1220*, 128704.
11. Venkatachalam, V., Ramalingam, K., Bocelli, G., & Cantoni, A. (1997). Influence of free and chelating phosphine on the NiS2P2 planar chromophore. Synthesis and single crystal structure determination of bis (triphenylphosphine)(N, N′-iminodiethylenebis (phthalimide)-dithiocarbamato) nickel (II) perchlorate, methanol and water solvate and [1, 2-

Journal of Chemical Health Risks

www.jchr.org

JCHR (2025) 15(6), 3498-3519 | ISSN:2251-6727

bis (diphenylphosphino-kP, P′) ethane]-(N, N′-iminodiethylenebis (phthalimide) dithiocarbamato) nickel (II) tetraphenylborate water solvate. *Inorganica chimica acta*, *257*(1), 49-58.

12. Prakasam, B. A., Ramalingam, K., Baskaran, R., Bocelli, G., & Cantoni, A. (2007). Synthesis, NMR spectral and single crystal X-ray structural studies on Ni (II) dithiocarbamates with NiS2PN, NiS2PC, NiS2P2 chromophores: Crystal structures of (4-methylpiperazinecarbodithioato)(thiocyanato-N)(triphenylphosphine) nickel (II) and bis (triphenylphosphine)(4-methylpiperazinecarbodithioato) nickel (II) perchlorate monohydrate. *Polyhedron*, *26*(5), 1133-1138.
13. Yadav, R., Trivedi, M., Kociok-Köhn, G., Prasad, R., & Kumar, A. (2015). New Ni (II) 1, 2-bis (diphenylphosphino) ethane dithiolates: crystallographic, computational and Hirshfeld surface analyses. *CrystEngComm*, *17*(47), 9175-9184.
14. Spek, A. L., Van Eijck, B. P., Jans, R. J. F., & Van Koten, G. (1987). Structure of dichloro [1, 2-bis (diphenylphosphino) ethane] nickel (II) dichloromethane solvate. *Crystal Structure Communications*, *43*(10), 1878-1880.
15. Thananatthanachon, T., & Lecklider, M. R. (2017). Synthesis of Dichlorophosphinenickel (II) Compounds and Their Catalytic Activity in Suzuki Cross-Coupling Reactions: A Simple Air-Free Experiment for Inorganic Chemistry Laboratory. *Journal of Chemical Education*, *94*(6), 786-789.
16. Shawish, H. B., Maah, M., Halim, S. N. A., & Shaker, S. A. (2016). Synthesis, characterization and structural studies of binuclear nickel (II) complexes derived from dihydroxybenzaldehyde thiosemicarbazones, bridged by 1, 2-bis (diphenylphosphino) ethane. *Arabian Journal of Chemistry*, *9*, S1935-S1942.
17. El-Khateeb, M., Tanash, Q., Abul-Futouh, H., Goerls, H., & Weigand, W. (2019). Dithiocarbonato nickel, palladium and platinum complexes bearing bis (diphenylphosphino) ferrocene: synthesis and X-ray structure determination. *Journal of Chemical Sciences*, *131*(10), 103.
18. Halim, S. N. A. A. (2020). A *Synthesis, Structure Elucidation and Selected Biological Activities of Ag (I) and Au (I) Complexes Constructed from Thiosemicarbazone and Phosphine Ligands* (Master's thesis, University of Malaya (Malaysia)).
19. Saiyed, T. A., Adeyemi, J. O., Saibu, G. M., Singh, M., Oyedeji, A. O., Hosten, E. C., & Onwudiwe, D. C. (2023). Bipyridine adducts of Zn (II) and Ni (II) bis (N-methyl-N-phenyl dithiocarbamate): Synthesis, characterization, and biological applications. *Journal of Molecular Structure*, *1274*, 134335.
20. Hameury, S., de Fremont, P., Breuil, P. A. R., Olivier-Bourbigou, H., & Braunstein, P. (2015). Bis (ether-functionalized NHC) nickel (II) complexes, trans to cis isomerization triggered by water coordination, and catalytic ethylene oligomerization. *Organometallics*, *34*(11), 2183-2201.
21. Kuveke, R. E., Barwise, L., van Ingen, Y., Vashisth, K., Roberts, N., Chitnis, S. S., ... & Melen, R. L. (2022). An international study evaluating elemental analysis.
22. Neto, W. P. F., Putaux, J. L., Mariano, M., Ogawa, Y., Otaguro, H., Pasquini, D., & Dufresne, A. (2016). Comprehensive morphological and structural investigation of cellulose I and II nanocrystals prepared by sulphuric acid hydrolysis. *Rsc Advances*, *6*(79), 76017-76027.
23. Kotlyar, V. (1997). NMR chemical shifts of common laboratory solvents as trace impurities. *The Journal of organic chemistry*.
24. Nakamoto, K. (2009). *Infrared and Raman spectra of inorganic and coordination compounds, part B: applications in coordination, organometallic, and bioinorganic chemistry*. John Wiley & Sons.
25. Lever, A. B. P., & Rice, S. A. (1969). Inorganic electronic spectroscopy.
26. Denney, R. C., Vogel, A. I., & Mendham, J. (2000). Vogel's textbook of quantitative chemical analysis/revised by J Mendham...[et al.].
27. Silverstein, R. M., & Bassler, G. C. (1962). Spectrometric identification of organic

compounds. *Journal of Chemical Education*, *39*(11), 546.

28. Harris, R. K., Becker, E. D., Cabral de Menezes, S. M., Goodfellow, R., & Granger, P. (2001). NMR nomenclature. Nuclear spin properties and conventions for chemical shifts (IUPAC Recommendations 2001). *Pure and applied chemistry*, *73*(11), 1795-1818.
29. Jiemuratova, A. A., ugli Khusanov, O. A., ugli Khalikulov, K. J., & ugli Pardayev, U. B. K. (2025). SYNTHESIS AND STRUCTURAL CHARACTERIZATION OF ACETONITRILE-COORDINATED ZN (II) AND CU (II) COMPLEXES WITH NON-COORDINATING ANIONS. *SHOKH LIBRARY*.
30. Cotton, F. A., Wilkinson, G., Murillo, C. A., & Bochmann, M. (1999). *Advanced inorganic chemistry*. John Wiley & Sons.
31. Socrates, G. (2004). *Infrared and Raman characteristic group frequencies: tables and charts*. John Wiley & Sons.
32. Tan, Y. S., Yeo, C. I., Tiekink, E. R., & Heard, P. J. (2021). Dithiocarbamate complexes of platinum group metals: Structural aspects and applications. *Inorganics*, *9*(8), 60.